

SCIENTIFIC REPORTS



OPEN

Single microtubules and small networks become significantly stiffer on short time-scales upon mechanical stimulation

Matthias D. Koch^{1,3}, Natalie Schneider², Peter Nick² & Alexander Rohrbach¹

The transfer of mechanical signals through cells is a complex phenomenon. To uncover a new mechanotransduction pathway, we study the frequency-dependent transport of mechanical stimuli by single microtubules and small networks in a bottom-up approach using optically trapped beads as anchor points. We interconnected microtubules to linear and triangular geometries to perform micro-rheology by defined oscillations of the beads relative to each other. We found a substantial stiffening of single filaments above a characteristic transition frequency of 1–30 Hz depending on the filament's molecular composition. Below this frequency, filament elasticity only depends on its contour and persistence length. Interestingly, this elastic behavior is transferable to small networks, where we found the surprising effect that linear two filament connections act as transistor-like, angle dependent momentum filters, whereas triangular networks act as stabilizing elements. These observations implicate that cells can tune mechanical signals by temporal and spatial filtering stronger and more flexibly than expected.

Today, we know that cells across all domains are mechanosensitive¹, and that mechanosensitivity is the base for sensing quite different stimulus qualities including osmotic challenges, gravity, movements or even sound. In addition, mechanosensitivity is used to organize and integrate cells and organs into functional units, e.g., in the course of movements in metazoan organisms or during plant development². Perturbations of mechanotransduction have been implicated in various severe diseases like cancer^{3,4}. Remodeling of the cell as a response or adaption to an external, physical stimulus is steered by gene expression in the nucleus⁵. Therefore, the information of the stimulus has to be transported across the cell from the periphery to the center. Common models of cellular mechanotransduction assume the conversion of a physical stimulus to a chemical signal by membrane proteins such as integrins³, and the subsequent transport to the nucleus either passively by diffusion or actively by molecular motors, i.e., rather slow processes. However, the direct propagation of a mechanical stimulus by stress waves through stiff cytoskeletal elements connecting the membrane and the nucleus⁶ would enable a much faster transport pathway on the microsecond timescale and thus allow almost instantaneous integration of responses across the cell⁷. A model for such a pathway has been proposed by Ingber^{8,9} on the basis of a tensegrity model of flexible actin filaments (able to transmit traction forces) connected to the relatively stiff microtubules (able to transmit compression forces). In mammalian cells, microtubules are typically aligned radially inside a cell spanning from the centrosome, located close to the nucleus, to the cell membrane¹⁰, a set up that would allow for efficient mechanotransduction between cell membrane and nucleus¹¹. In fact, mechanical stimulation has been shown recently to induce a perinuclear actin ring, brought about by the activity of actin-microtubule cross-linking formins¹². MTs are well known as components of mechanosensing in flies¹³ as well as in vertebrates¹⁴ and microtubules have also been found to participate in gravity sensing and mechanic integration in plants (reviewed in ref. 15). Remarkably, mutants of *Caenorhabditis* affected in beta tubulin turned out to be

¹Laboratory for Bio- and Nano-Photonics, Department of Microsystems Engineering, University of Freiburg, Georges-Koehler-Allee 102, 79110, Freiburg, Germany. ²Molecular Cell Biology, Botanical Institute, Karlsruhe Institute of Technology, Fritz-Haber-Weg 4, 76131, Karlsruhe, Germany. ³Present address: Lewis-Sigler Institute for Integrative Genomics, Princeton University, Washington Rd, Princeton, NJ, 08544, USA. Correspondence and requests for materials should be addressed to A.R. (email: rohrbach@imtek.de)

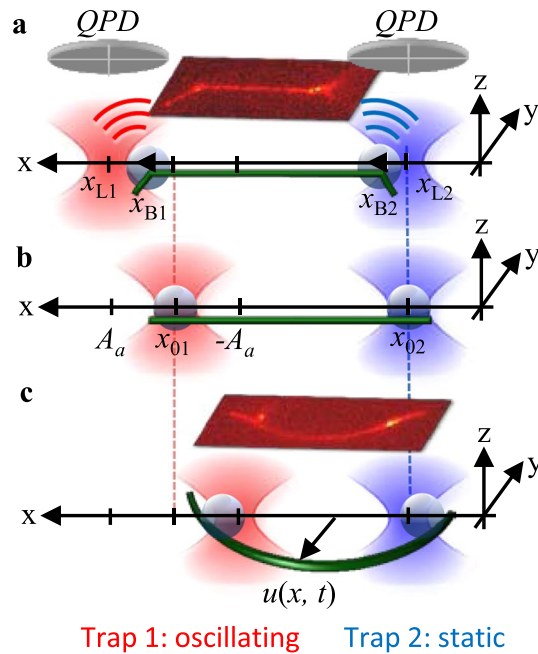


Figure 1. Design of experiment illustrating different stages of an oscillation period. Optically trapped $d = 1.06 \mu\text{m}$ Neutravidin-coated beads are used as anchor points for laterally attached, biotinylated microtubules. Bead positions are tracked interferometrically by QPDs. **(a)** The filament is stretched during the first half oscillation period. **(b)** The filament is straight after each half period. **(c)** The filament is buckled during the second half oscillation period. Insets: overlay of corresponding fluorescence and brightfield images.

insensitive to mechanic stimulation¹⁶. Efficiency and specificity of the MT sensory functions, however, depend on their frequency dependent viscoelastic properties, which are characteristic for biological systems.

To address these aspects of microtubule-dependent signaling, we present an approach for the targeted construction of cytoskeletal meshes with defined geometries by using optically trapped beads as anchor points. Existing approaches only demonstrated the construction of small networks without biologically relevant measurements¹⁷ or rely on the stochastic attachment or growth of filaments to optically trapped beads or micro pillars which is less flexible and barely allows control of the number of attached filaments^{18–20}. We use established micro-rheology techniques^{21–23} to measure the time-dependent viscoelastic properties of single microtubules. Existing approaches have investigated bulk material properties^{24–26} *in vitro*, the properties of the cytoskeletal molecules *in vivo*²⁷ ignoring their organization or number^{28–30}, or static representations of single filaments^{31,32}. Microtubule stiffness and bending relaxation has also been addressed by Fourier decomposition of bending modes caused by thermal fluctuation^{33,34}, however, thermal forces are not sufficient in amplitude to significantly deform a whole network. A recent review summarizing the molecular origins of microtubule mechanics and highlighting effects of network architecture during stress transmission is presented by Lopez and Valentine³⁵.

Since different cell types show different structures of the cytoskeleton and alignment of microtubules, we test the viscoelastic properties of different small network topologies on their performance of conducting mechanical stimuli at different frequencies. This approach should not only allow determining which network symmetries are best suited to transduce mechanical signals, but also to get insight into the general role of the cytoskeletal structure and function in different cell types by successively increasing the complexity of the network through addition of other cytoskeletal associated components.

Results

To determine the time-dependent viscoelastic properties of single microtubules (MTs) and small networks of MTs, movable Neutravidin coated beads as anchor points were attached to a biotinylated microtubule at defined positions by time-shared optical tweezers (see Methods). Then, these anchor points were mutually displaced in an oscillatory fashion with defined frequencies and amplitudes along the x-direction as illustrated in Fig. 1. The resulting frequency dependent stretching and buckling behavior of these constructs is measured, which allows determining both the elastic and the viscous properties of the MT constructs in different geometrical arrangements.

Stiffening of single filaments at high oscillation frequencies. Upon force generation, the beads are displaced from their equilibrium position with a straight microtubule as depicted in Fig. 1. The displacements $x_{B1}(t) - x_{L1}(t)$ and $x_{B2}(t) - x_{L2}(t)$ of bead 1 (actor) and bead 2 (sensor) relative to the laser trap positions x_{L1} and x_{L2} , are shown exemplarily in Fig. 2a,b for two different actor displacement frequencies, $f_a = 0.1$ Hz and $f_a = 100$ Hz, at a displacement amplitude $A_a = 500$ nm. Due to high tensile and small buckling forces, the sensor bead is pulled out of the trap center by up to $x_{B2} \approx 80$ nm and pushed only slightly by less than $x_{B2} \approx 10$ nm during

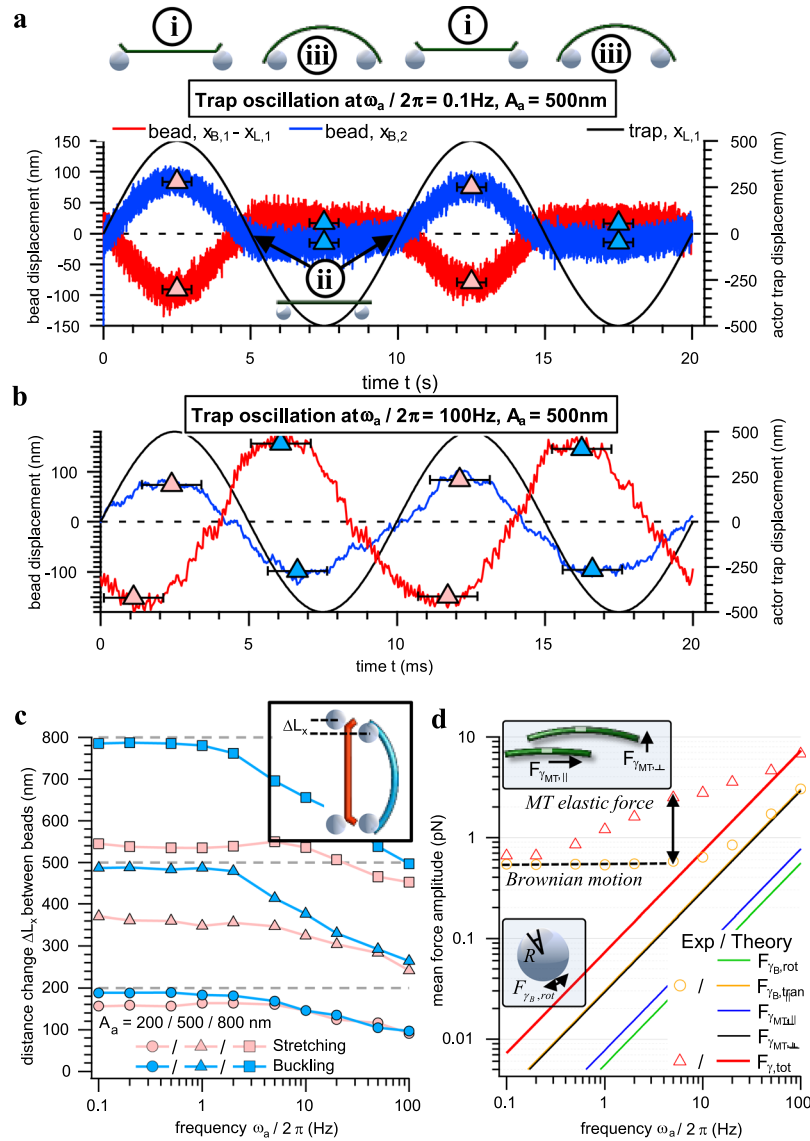


Figure 2. Frequency dependent response of a single microtubule filament – bead construct ($L = 5 \mu\text{m}$). **(a)** and **(b)** Two periods of the relative actor and sensor bead displacements $x_{B1}(t) - x_{L1}(t)$ and $x_{B2}(t) - x_{L2}(t)$ from their trap centers during oscillations of the actor trap $x_{L1}(t) = L/2 + A_a \sin(\omega_a t)$ and the static sensor trap $x_{L2}(t) = -L/2$ at $A_a = 500 \text{ nm}$ and $\omega_a/2\pi = 0.1 \text{ Hz}$ **(a)**, or $\omega_a/2\pi = 100 \text{ Hz}$ **(b)**, respectively. Markers indicate the maximum amplitude x_{max1} and x_{max2} of both beads during each half period. **(c)** Frequency dependence of the maximum amplitude $\Delta L_x = A_a - x_{max1} - x_{max2}$ between both beads during stretching and buckling averaged over several oscillation periods. **(d)** Theoretical mean amplitudes of the involved viscous forces (solid lines) compared to the experimentally obtained sum of all acting forces (markers) for a single trapped bead (yellow) and the filament – bead construct (red).

each half period. This situation changes significantly at high frequencies $f_a = 100 \text{ Hz}$. While the maximum displacements x_{B2} during microtubule stretching were approximately the same at $f_a = 100 \text{ Hz}$ and $f_a = 0.1 \text{ Hz}$, the displacement increased by an order of magnitude at high frequencies during buckling, i.e., $x_{B2}(f_a = 100 \text{ Hz}) \approx 10 \cdot x_{B2}(f_a = 0.1 \text{ Hz})$. Therefore, only the compression and buckling of single filaments will be analyzed in this study. The complete frequency dependence of the filament – bead construct is expressed by the average maximum distance change between both beads $\Delta L_x = A_a - x_{max1} - x_{max2}$ as shown in Fig. 2c for three different amplitudes A_a during stretching and buckling. While the slight amplitude decrease during stretching can be attributed to the increasing friction force $F_{\gamma,B} = 6\pi R\eta\dot{x}_B$ of the bead, the much stronger drop during buckling is caused by the microtubule filament, indicating an apparent stiffening of the filament at high oscillation frequencies $f_a > 1 \text{ Hz}$ (see Supplementary Results Fig. S2). We would like to point out that microtubules are inextensible and not actually stretched during the pulling phase³². Instead, they are bent locally as shown in Fig. 1a. To estimate whether this frequency response is a purely viscous effect governed by the friction of the actuated filament, we analyzed the amplitudes of the involved forces theoretically as explained in the Supplementary Results and shown in Fig. 2d. The main contributions to the amplitude of the total viscous force $F_{\gamma,tot} \approx F_{\gamma,B,tran} + F_{\gamma_{MT},\perp}$ are the trans-

lational viscous forces of the beads $F_{\gamma_B,tran}$ and the perpendicular viscous force component of the filament $F_{\gamma_{MT},\perp}$. Both, the rotational viscous forces of the beads $F_{\gamma_B,rot}$, acting as hinged supports of the filament ends, and the parallel viscous forces $F_{\gamma_{MT},\parallel}$ are negligible. A comparison between the theoretically estimated viscous and the experimentally obtained total force amplitudes reveals a strong difference especially dominant at intermediate frequencies $1\text{ Hz} \leq f_a \leq 100\text{ Hz}$. This shows that significant elastic forces control the deformation of the microtubule filament.

Excitation and relaxation of higher MT deformation modes. As introduced above, the oscillatory driving force counteracts against the viscous and the elastic forces of both the MT and the two beads. The behavior of the semi-flexible MT of length L is described by the hydrodynamic beam equation, which predicts that induced MT deformations can be described by a superposition of sine waves with wave numbers $q_n = \frac{n \cdot \pi}{L}$ and a characteristic relaxation time proportional to $1/q^4 \sim L^4$ (see Methods and Supplementary Results). Hence, higher deformation modes $n > 1$ can only be excited at higher driving frequencies $\omega = 2\pi f_a$, leading to the effect of MT stiffening. The stiffening can be described by the frequency dependent complex shear modulus $G(\omega) = G'(\omega) + i \cdot G''(\omega)$ (see Methods Section), where a representation of all forces in frequency space allows to extract the elastic component $G'(\omega)$ and the viscous component $G''(\omega)$.

The elastic modulus $G'(\omega)$ shown in Fig. 3 describes the frequency dependent MT stiffness, which is characterized by a constant plateau value $G'(0)$ and a frequency dependent response $G'(\omega \gg \omega_1)$ at high frequencies. This can be estimated as

$$G'(\omega = 0) = \frac{\pi^2}{2.16} \cdot \left(\frac{1}{L}\right)^4 \ell_p k_B T \text{ and } G'(\omega > \omega_1) \sim \omega^p \quad (1)$$

Here, $\ell_p = EI/k_B T$ is the persistence length of a semiflexible polymer with $L \ll \ell_p$ and bending modulus EI (flexural rigidity). The frequency of the MT's ground mode $\omega_1 = \frac{EI}{g_{MT}} \left(\frac{\pi}{L}\right)^4$ depends on the viscous drag g_{MT} of the MT. As shown further below, we obtain a power law exponent $p = 5/4$ for oscillations of single microtubules in longitudinal direction, matching the theoretical prediction for semiflexible filaments in the intermediate frequency regime^{36,37} tested here. However, we also find that the degree of stiffening, the exponent p , depends on the filament stabilization, i.e., the molecular architecture of the filament, and the direction of oscillation.

We checked whether the measured frequency response and apparent stiffening of single filaments indeed results from the excitation of higher deformation modes as described by Equation (1). Therefore, we analyzed the dynamics of the trapped anchor points with two particle active micro-rheology techniques (see refs 22, 23 and Supplementary Methods for details) as described in the following.

The frequency dependent elastic response of the single microtubule was analyzed in terms of $G'(\omega)$. As explained in the Supplementary Information, we can assume proper linear response for all of the mentioned experimental conditions. The results for filaments stabilized with Taxol and polymerized with either GTP or its slowly hydrolysable homolog GMPCPP are displayed in Fig. 3a–c. Here, the results are grouped according to lengths $L \approx 5\ \mu\text{m}$ ($3.4\ \mu\text{m} \leq L \leq 6.0\ \mu\text{m}$ for Taxol) and $L \approx 15\ \mu\text{m}$ ($15\ \mu\text{m} \leq L \leq 25\ \mu\text{m}$ for Taxol and $10\ \mu\text{m} \leq L \leq 16\ \mu\text{m}$ for GMPCPP). Each group represents the average of 3–6 individual filaments each probed at 2–4 different oscillation amplitudes ($A_a = 200\ \text{nm}$, $400\ \text{nm}$, $600\ \text{nm}$ typically), resulting in approximately 10 measurements per group. The grouping was chosen due to the length dependence of the persistence length^{34,38}, as discussed further below, and because no significant difference in elasticity within these individual groups could be observed. For an oscillation parallel to the filament axis, the theoretical slope with $p = 1.25$ according to Equation (1) (also see Methods) fits well to our experimental results as shown in Fig. 3a–c. However, we also used a free exponent p as additional fit parameter, $G'(\omega) - G'(0) = C\omega^p$, to check for any deviation from the theoretical prediction. We obtained $p = 1.08 \pm 0.15$ and $p = 0.93 \pm 0.07$ for short and long MTs stabilized by $10\ \mu\text{M}$ Taxol, $p = 0.78 \pm 0.25$ and $p = 1.46 \pm 0.13$ for short and long MTs stabilized by $100\ \mu\text{M}$ Taxol, and $p = 1.51 \pm 0.13$ for (long) GMPCPP filaments. Within the error margins this indicates a rough coincidence with our model ($p = 0.75$) for short MTs, whereas the stiffening for longer MTs better matches with the advanced model^{36,37} predicting an exponent $p = 1.25$.

Frequency response depends on MT stabilizations. *Frequency dependent persistence length.* Figure 3a–c show that the plateau value depends on the length of the filament and filament stabilization. For long filaments ($L \approx 15\ \mu\text{m}$) we find $G'(0) = 1.5\ \text{mPa}$ (with $10\ \mu\text{M}$ Taxol), $G'(0) = 2\ \text{mPa}$ (with $100\ \mu\text{M}$ Taxol) and $G'(0) = 4\ \text{mPa}$ (with GMPCPP). For short filaments ($L \approx 5\ \mu\text{m}$), MT stabilization hardly affects the plateau values, which are $G'(0) \approx 10\ \text{mPa}$ for both $10\ \mu\text{M}$ and $100\ \mu\text{M}$ Taxol. No data is available for short GMPCPP filaments. As shown in Equation (1), the plateau value is a measure of the persistence length. Dividing $G'(\omega)$ by $\frac{\pi^2 k_B T}{2.16 \cdot L^4}$, we find a frequency dependent persistence length

$$\ell_p(\omega) = G'(\omega) \cdot \frac{2.16}{k_B T \pi^2} L^4 \approx \ell_p(0) + \ell_p(\omega > \omega_1) \quad (2)$$

which increases with frequency because of a successive excitation of higher modes at $\omega > \omega_1$.

It can be seen in Fig. 3d that the persistence length depends sensitively on the contour length L of the MT. We find $\ell_p(0) = (0.33 \pm 0.05)\ \text{mm}$ for $L = 5\ \mu\text{m}$ and all stabilizations. For $L = 15\ \mu\text{m}$ we find $\ell_p(0) = (4.06 \pm 0.26)\ \text{mm}$ stabilized with $10\ \mu\text{M}$ Taxol, $\ell_p(0) = (5.80 \pm 0.39)\ \text{mm}$ for $100\ \mu\text{M}$ Taxol, and $\ell_p(0) = (12.10 \pm 0.66)\ \text{mm}$ for GMPCPP. The estimates based on Equation (2) agree well with the published dependency of ℓ_p on the filament contour length³⁸ and stabilization³⁹, as further elucidated in the discussion.

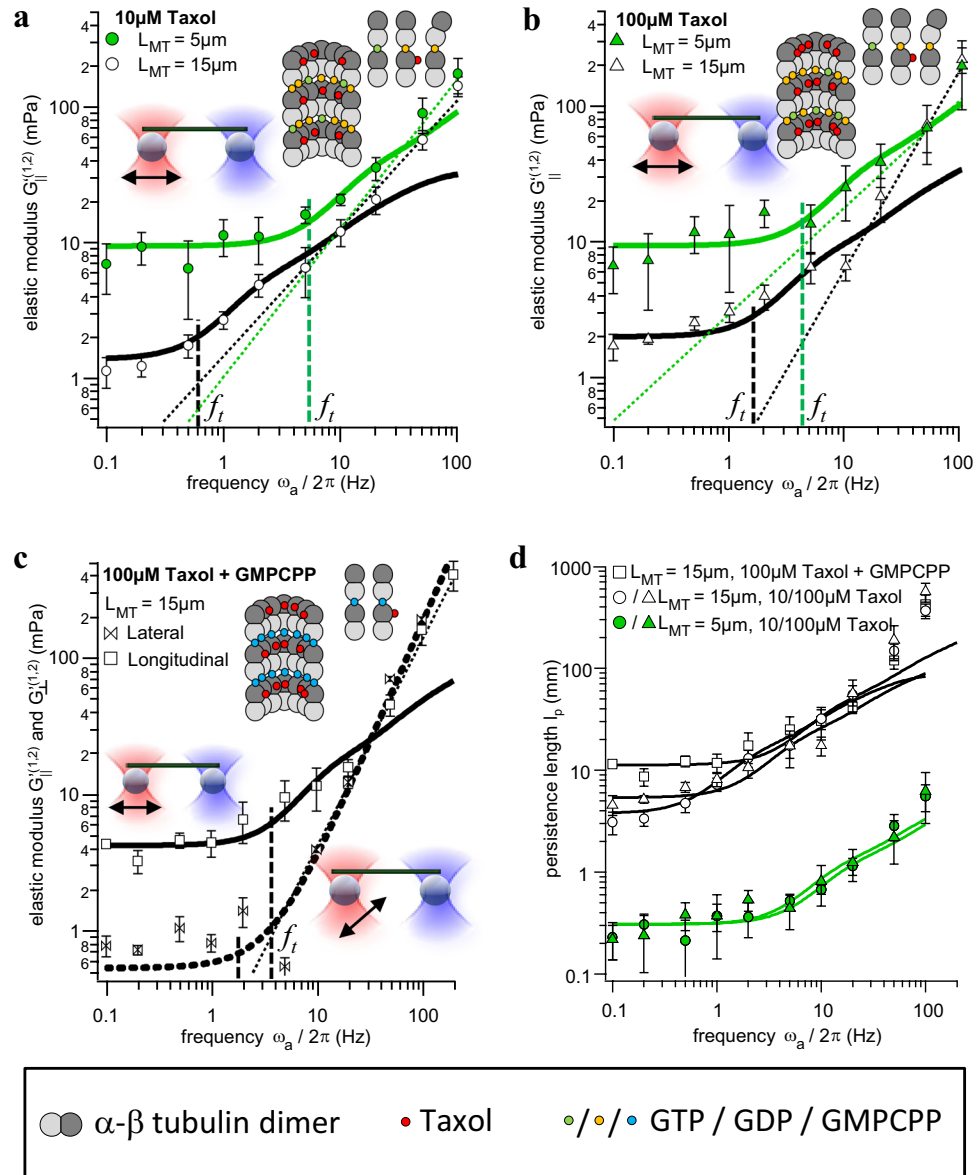


Figure 3. Elastic modulus for differently stabilized single microtubules of different lengths. (a) Stabilization with 10 μM Taxol, MT end oscillation direction: longitudinal. $N = 8$ measurements for short and $N = 19$ measurements for long microtubules. (b) Stabilization with 100 μM Taxol, MT end oscillation direction: longitudinal. $N = 9$ measurements each length. (c) Stabilization with GMPCPP + 100 μM Taxol, MT end oscillation directions: longitudinal (solid black line) and lateral (dashed black line). $N = 9$ measurements each direction. (d) Frequency dependent persistence lengths obtained from the elastic moduli for all filament types. Error bars represent the standard deviation (SD).

Transition frequency. Beyond a characteristic frequency, a visible increase of $G'(\omega)$ is manifested due to the excitation of higher deformation modes. We define this transition by the frequency ω_t where $G'(\omega_t)/G'(0) = 1.5$, i.e., $G'(\omega)$ is increased by 50% such that

$$\omega_t \approx 3\omega_1 = \frac{3}{g_{\text{MT}}} \left(\frac{\pi}{L}\right)^4 \ell_p(0)kT \quad (3)$$

We find that the transition frequency $\omega_t = 2\pi f_t$ scales by a factor of 3 with the ground mode.

We obtain $f_t = (5.3 \pm 1.2)$ Hz and $f_t = (4.2 \pm 1.7)$ Hz for short filaments ($L = 5 \mu\text{m}$) stabilized with 10 μM or 100 μM Taxol, respectively. For long filaments ($L = 15 \mu\text{m}$), we find $f_t = (0.6 \pm 0.1)$ Hz, $f_t = (1.8 \pm 0.4)$ Hz and $f_t = (3.9 \pm 0.8)$ Hz for stabilization with 10 μM , or 100 μM Taxol, or for 100 μM Taxol + GMPCPP, respectively. Comparing this to the theoretical estimate of Equation(3) predicting $\omega_t = 21$ Hz and $\omega_t = 35$ Hz for short MTs with 10 μM and 100 μM and $\omega_t = 2$ Hz, $\omega_t = 3.3$ Hz and $\omega_t = 7$ Hz for long MTs with 10 μM , 100 μM and GMPCPP, our experimentally obtained values are throughout too small, but follow the general dependence on length and stiffness (see Supplementary Results Fig. S11). Thus, the transition frequency ω_t increases

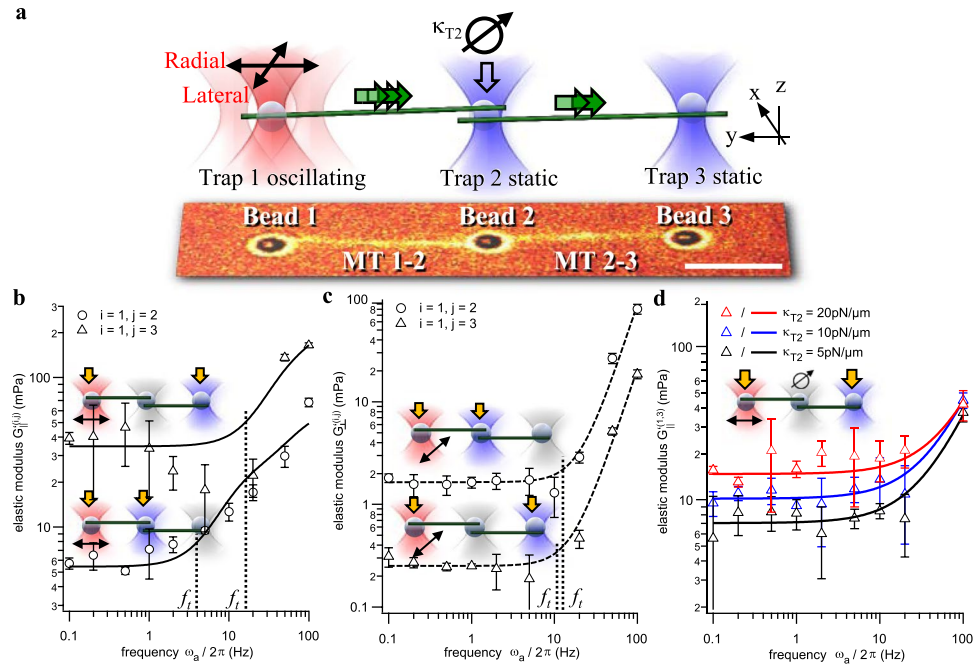


Figure 4. Rheology of a linear chain of connected filaments with transistor function. **(a)** Experimental design of linear network of two filaments held by three trapped beads. Bottom: overlay of fluorescence and brightfield image. Scale bar: 5 μm . **(b)** and **(c)** Elastic components G' for a longitudinal and lateral MT end oscillation, i.e., in directions longitudinal or lateral to filaments, respectively. The transition frequencies are marked by black dotted lines. **(d)** Elastic components $G'_{||}^{(1,3)}$ for a longitudinal oscillation and different stiffnesses κ_{T2} of the intermediate optical trap. Error bars represent the standard deviation (SD) of $N = 3$ measurements each.

with increasing stabilization, clearly indicating the importance of the molecular structure of microtubules (see Discussion). As indicated in Fig. 3a–c (vertical dashed lines), these results fit well to a graphical estimation of f_t at $G'(\omega_t) = 1.5 \cdot G'(0)$.

Lateral oscillation of single filaments. So far, only longitudinal oscillations of filament ends have been considered, i.e. bead displacements parallel to the filament axis. Figure 3c further shows the result for a bead oscillation lateral to the axes of long ($L = 15 \mu\text{m}$) GMPCPP stabilized filaments. Again, we observe a plateau value for frequencies $\omega < \omega_t$ and a power law rise for $\omega > \omega_t$ with $p = 1.76 \pm 0.02$, i.e., a 40% larger stiffening exponent than the predicted value $p = 1.25$ for a longitudinal oscillation. In contrast, the plateau $G'_{\perp}(0) = 0.54 \text{ mPa}$ is approximately one order of magnitude smaller than $G'_{||}(0)$ in axial direction. The transition frequency $f_t = 3 \text{ Hz}$ obtained from $G'_{\perp}(\omega_t) = 1.5 G'_{\perp}(0)$ is approximately the same as in axial direction.

Momentum transport along a linear chain of connected MTs. An important question is whether the findings for single filaments can be used to predict the momentum transport through small networks of filaments - in analogy to Kirchhoff's circuit laws for the connection of currents in network nodes. However, for connected microtubules, i.e. for different networks, the compression of one filament usually results in a stretching of another filament and vice versa, such that a separation of compression and stretching is not possible anymore. Therefore, the complete oscillation period of the actor and sensor beads will be analyzed in the following.

In a first step, we constructed a linear network consisting of three optically trapped beads and two microtubule filaments as shown in Fig. 4a. This construct was probed such that trap 1 was oscillated sinusoidally at varying frequency and amplitude, while trap 2 and 3 remained stationary. In this way, we investigated the momentum transfer along the first microtubule, while attached to a second microtubule, through $G'^{(1,2)}(\omega)$, but also the momentum transfer along both microtubules through $G'^{(1,3)}(\omega)$. The longitudinal and lateral oscillation of the actor and sensor beads displayed in Fig. 4b,c reveal a qualitatively similar momentum transfer as for single filaments. Results are the average of three measurements for filaments of length $L = 10 \mu\text{m}$ after stabilization with $100 \mu\text{M}$ Taxol.

Longitudinal chain oscillation. By inspecting the curves in Fig. 4b,c, both a frequency-independent plateau $G'^{(i,j)}(0)$, and a frequency-dependent behavior $G'^{(i,j)}(\omega)$ between beads i and j can be observed. Using power law fits according to Equation (1), the plateau values $G'^{(1,2)}(0) = 6 \text{ mPa}$ and $G'^{(1,3)}(0) = 32 \text{ mPa}$ for a single ($1 \rightarrow 2$) and two-step ($1 \rightarrow 3$) MT connection are determined. Interestingly, the static elasticity $G'^{(1,3)}(0) > G'^{(1,2)}(0)$ for the two step connection is larger than for the single step. As shown in Fig. 4d, $G'^{(1,3)}(0, \kappa_{T2})$ is a function of the stiffness κ_{T2} of the intermediate trap 2. Here, we repeated the measurement and doubled the trap stiffness κ_{T2} each

time, resulting in an increase of $G^{(1,3)}(0) \sim \sqrt{\Delta\kappa_{T2}}$ proportional to the square root of the stiffness change $\Delta\kappa_{T2}$. While $G^{(1,2)}(0)$ for the first 10 μm long filament fits well between $G'(0)$ for $L = 5 \mu\text{m}$ and $L = 15 \mu\text{m}$ shown above, $G^{(1,3)}(0)$ for two 10 μm long filaments is much larger than $G'(0)$ for a single filament with $L = 20 \mu\text{m}$

The transition frequency $f_t^{(1,2)} = (4.1 \pm 0.3)$ Hz (black dashed line in Fig. 4b) according to $f_t = \frac{1}{2g_{MT}} \left(\frac{\pi}{L}\right)^4 \ell_p(0)kT$ in Equation (3) is approximately identical to that of single filaments, while $f_t^{(1,3)} = (17 \pm 2.5)$ Hz is approximately 4 times larger.

Lateral chain oscillation. As shown in Fig. 4b,c, the static elasticity $G'(0)$ for lateral displacements of beads and MT ends is significantly different to longitudinal (parallel) displacements. For the longitudinal elasticity $G_{\parallel}^{(i,j)}(0)$, the double MT connection $1 \rightarrow 3$ was about five times stiffer than the direct MT connection $1 \rightarrow 2$, whereas for the lateral elasticity $G_{\perp}^{(i,j)}(0)$, the connection $1 \rightarrow 3$ is about five times softer than the connection $1 \rightarrow 2$, i.e., $G_{\perp}^{(1,3)}(0) \approx \frac{1}{5}G_{\perp}^{(1,2)}(0)$. Beyond the transition frequency, the frequency dependent elasticity $G_{\perp}^{(i,j)}(\omega) \sim \omega^p$ increases according to a power law exponent $p = 2.5 \pm 0.1$ and $p = 2.4 \pm 0.1$ for the connection $1 \rightarrow 2$ and $1 \rightarrow 3$. Interestingly, the transition frequency $f_t = (11 \pm 1)$ Hz is approximately the same for both connections, in contrast to the longitudinal oscillations. However, during a lateral oscillation, both filaments are always slightly stretched compared to a longitudinal oscillation, where filaments are buckled. The role of the intermediate connection and the role of the coupling point (trapped bead #2) are explained in the discussion.

Momentum transport in an equilateral triangle. We used GMPCPP filaments to construct equilateral triangles of 15 μm side length as depicted in Fig. 5a. The trap 1 is again oscillated in x or y , resulting in a trap movement radial or tangential to the connection between bead 1 and the center of the triangle. An overlay of brightfield and fluorescence images of one radial oscillation period at $f_a = 0.1$ Hz ($T = 1/f_a = 10$ s) and $A_a = 600$ nm along x is shown in Fig. 5b. In contrast to single filaments and the linear chain, here, in total two filaments are always buckled or tense, while at the same time, the third one behaves in the opposite manner, i.e., is tense or buckled.

Triangles are stiffer than single filaments and have a similar high frequency response. Due to the symmetric configuration of the equilateral triangle, the elastic modulus for both connections $1 \rightarrow 2$ and $1 \rightarrow 3$ should be identical, except for different oscillation directions. This is indeed the case as shown in Fig. 6a,b for an exemplary construct, where the radial and tangential elastic responses, $G_x^{(i,j)}(\omega)$ and $G_y^{(i,j)}(\omega)$, are plotted for an actor bead oscillation along x and y . The static elasticities $G_x^{(1,2)}(0) \approx G_x^{(1,3)}(0) = (55 \pm 20)$ mPa and $G_y^{(1,2)}(0) \approx G_y^{(1,3)}(0) = (30 \pm 10)$ mPa indicate a 25-fold increase of the overall stiffness of the construct compared to that of single filaments (see to Fig. 3c). In the Supplementary Results, we present further data of triangular constructs with slight pretension, induced by thermal fluctuations of the filaments during construction of the network.

According to Equation (3), the larger static elasticities should result in an increase of the transition frequency ω_t by a factor 25, i.e., $f_t = (810 \pm 308)$ Hz and $f_t = (75 \pm 13)$ Hz for both oscillation directions. 810 Hz is much larger than the measured maximum frequency, so that we cannot observe a power law rise for an oscillation along x . However, the extrapolated intersection of the single filament response (fit with free exponent according to Equation (1)) with the plateau of the triangle can be estimated to $f_t \approx 800$ Hz, which is in good agreement with the theoretical estimate of Equation (3). For the tangential oscillation direction (y) displayed in Fig. 6b, the network stiffens already at a transition frequency $f_t \approx (100 \pm 10)$ Hz (vertical black dashed line). This value is slightly larger than predicted (vertical red dashed line), which could be a consequence of the dip in $G'(\omega)$ at $f = 50$ Hz and might influence the value of f_t . This dip is not visible for other constructs with the same geometry as presented in the Supplementary Results.

Discussion

Microtubule stiffness depends on the contour length. We have analyzed the elastic behavior of single and inter-connected MTs by means of the elastic modulus $G'(\omega)$, which can be described by a low frequency plateau $G'(0) \sim \ell_p(0)$, and a rise at high frequencies above a characteristic transition frequency ω_t , defined by a 50% increase of $G'(\omega)$.

Varying the molecular composition of the filaments, by stabilization agents had no visible effect on the static elasticity of short MTs (5 μm length). Interestingly, this was different for long MTs (of around 15 μm length), where the effect of chemical stabilization on elasticity became visible, leading to the conclusion that the molecular coupling length extends over several μm . Similar effects have already been reported by Pampaloni *et al.*³⁸, who found a length dependence of the persistence length, which levels to a plateau above a critical length $\ell_c = 21 \mu\text{m}$, i.e., $\ell_p(L > \ell_c) = \text{const}$. Similarly, Taute *et al.*⁴⁰ introduced an additional internal friction term to explain deviations of their measured MT drag coefficients when microtubules were shorter than $\approx 5 \mu\text{m}$, attributed to dissipation during conformational changes or liquid flow passing through narrow pores in the MT lattice as introduced by⁴¹. Polymorphic conformational states of the tubulin lattice and non-equilibrium filaments dynamics have also been studied in motor based microtubule gliding assays, recently^{42,43}. Irrespective of the effects found here, the plateau value $G'(\omega = 0)$ is directly related to the conventional, frequency independent persistence length $\ell_p(\omega = 0)$, which increases with the contour length of the MTs according to $\ell_p(\omega = 0, L) \sim 1/(1 + \ell_c^2/L^2)$ ³⁸. We measured two different ranges of lengths for single MTs varying in length by a factor of 3 (plus one intermediate length for the linear network). Considering the total length dependence $G'(0) = \frac{kT\pi^2}{2.16} \ell_p(0, L) \left(\frac{\pi}{L}\right)^4 \sim \left(\frac{1}{L}\right)^2$, which is approximately quadratic and results in a 9-fold higher plateau for 3-fold shorter MTs, we find a reasonable match with

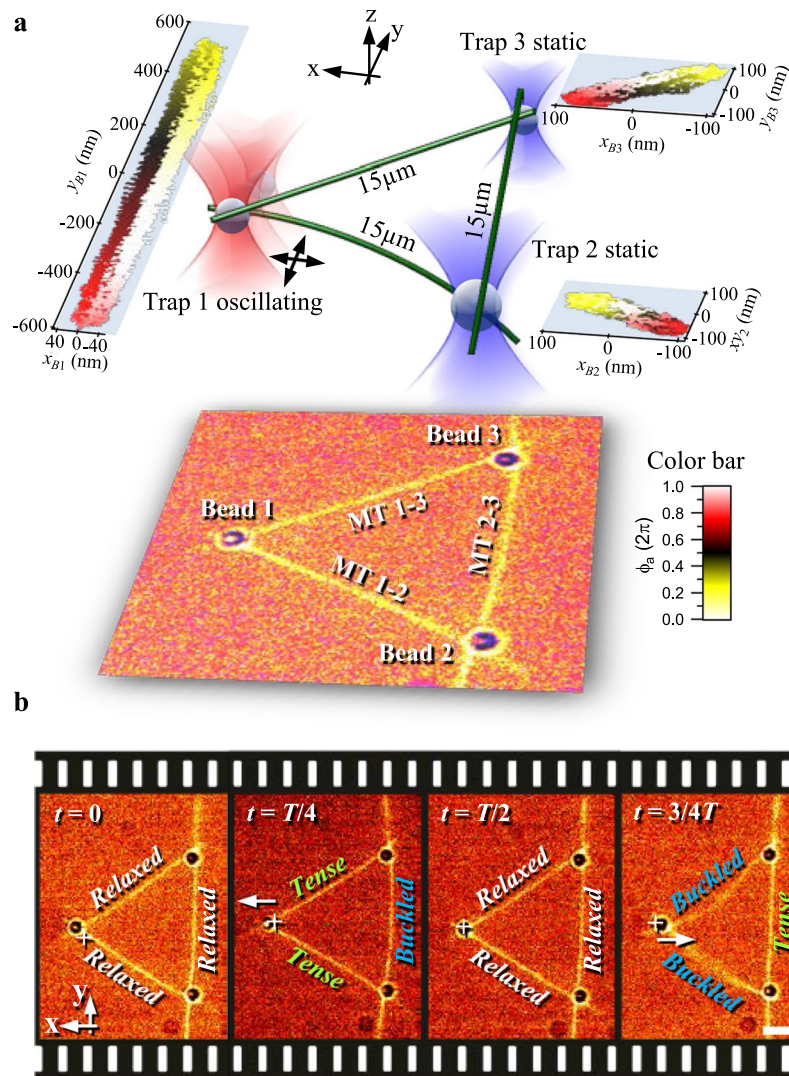


Figure 5. Probing an equilateral triangular network of GMPCPP filaments. **(a)** Design of experiment in pseudo 3D with overlay of fluorescence and brightfield image (bottom). Scatterplots of absolute bead positions during a tangential oscillation in y direction are shown color coded over the current phase ϕ_a of the actor trap. **(b)** Overlay of fluorescence and brightfield images of the characteristic time points during one radial (x) oscillation period at $f_a = 0.1$ Hz. Scale bar: $5 \mu\text{m}$.

our measurements shown in Fig. 3. From the two MT lengths, we also find that our results for $\ell_p(0, L)$ agree well to those reported previously^{34, 38}.

Frequency dependent persistence length and stiffness. The novelty of our observations is the increase of the persistence length, or correspondingly the elastic modulus $G'(\omega)$, of a single microtubule with the displacement frequency ω (Fig. 3). In the Methods section, we show that this is caused by the excitation of higher deformation modes, which means that filaments become stiffer on shorter timescales, such that filament buckling is suppressed. In other words, molecular relaxation processes as a consequence of internal stress along the MT cannot follow on too short timescales. The timescale of molecular relaxation is approximated by the transition frequency $\omega_t \approx 3 \cdot \omega_{n=1}$, which we indicated in all plots of $G'(\omega)$. Beyond this frequency, the second deformation mode ($n=2$) renders the filament about 1–4 times stiffer, beyond $\omega = 20 \cdot \omega_{n=1}$ the third deformation mode ($n=3$) stiffens the filament 4–10 times relative to $\omega = 0$ as explained in the Supplementary Results (Fig. S4). Our measurements confirm the general, theoretically predicted trend of a smaller transition frequency for longer MTs. According to $\omega_t = \frac{3kT}{g_{MT}} \ell_p(0) \left(\frac{\pi}{L}\right)^4 \sim \left(\frac{1}{L}\right)^2$, we expect an about 9-fold lower transition frequency for 3-fold longer MTs (see Methods), which we obtain for $10 \mu\text{M}$ Taxol stabilization, but not for $100 \mu\text{M}$ Taxol, indicating that further theoretical studies are necessary.

For short MTs we measured a stiffness increase according to $G'(\omega) \sim \omega^{3/4}$ at high frequencies ($50 \text{ Hz} < \omega < 100 \text{ Hz}$), whereas for longer MTs we found $G'(\omega \gg \omega_t) \sim \omega^{5/4}$, which is reasonably close to the theoretical prediction based on the hydrodynamic beam model for semiflexible filaments^{36, 37}. In some cases, though, such as for the strong GMPCPP stabilization, the fitting of a free exponent describes a power law

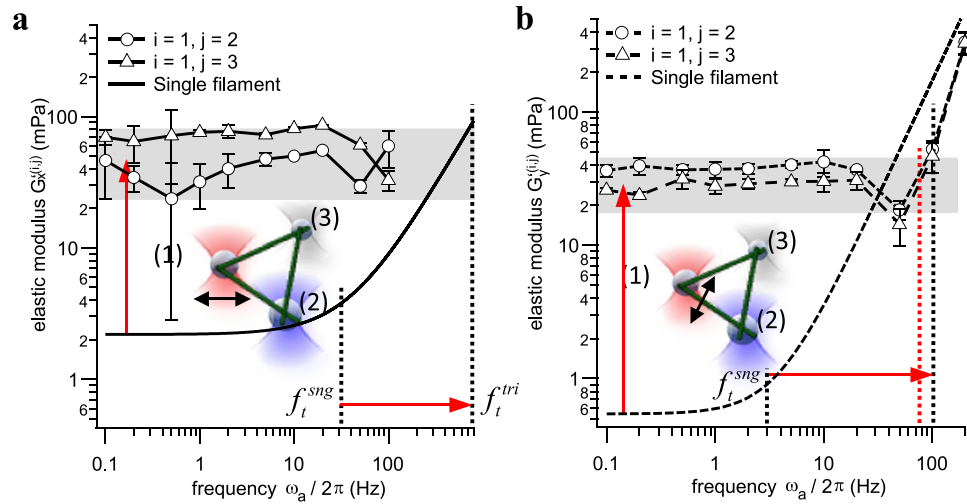


Figure 6. Elastic components $G'(\omega)$ for an equilateral triangular network. These are compared to the theoretical estimates for single filaments (lines without markers). **(a)** Radial oscillation along x . **(b)** Tangential oscillation along y . Error bars represent the standard deviation (SD) of $N = 10$ measurements each.

behavior of $\omega^{1.5}$, which represents faster stiffening, i.e., a slower molecular relaxation on shorter timescales. It is known that MTs polymerized in the presence of slowly or non-hydrolyzable GTP analogs such as GMPCPP or γ -S-GTP form more lateral inter-prot filament contacts between β -tubulins as compared to GTP/GDP MTs (see refs 44–46 and the Supplementary Material). Approximating the connection between individual $\alpha\beta$ -tubulin dimers by damped harmonic springs^{47, 48}, the damping of the intermolecular connections should affect the temporal response to mechanical stimuli and thereby the transition frequency ω_t .

Within the accuracy of our measurements, the viscous modulus $G''(\omega)$ (see Supplementary Results) increases linearly with frequency as predicted by the lateral friction coefficient $g_{MT} \cdot \omega = \frac{4\pi\eta\omega}{\ln(L/D) + 0.84}$ of a simple rod moving in an aqueous solution. Hence, we can clearly exclude that the strong increase of filament stiffness G' at high frequencies is governed by simple friction on the filament.

In biological and other noisy systems, the signal energy stored in various degrees of freedom (translation, oscillation, etc.) is significantly less pronounced at higher frequencies (e.g., a $1/\omega^2$ decay for thermal motion). In this way, microtubules should act as transmission amplifiers or high pass filters for mechanical signals, based on our observations that mechanical stimuli are transferred much more efficiently at higher frequencies.

Angular momentum filtering in a linear MT chain. For the linear MT chain, the MT triangle and for comparisons with single filaments, we analyze the full oscillation period of the anchor points leading to compression and stretching of the filaments. The serial connection of two $10\ \mu\text{m}$ microtubules (stabilized by $100\ \mu\text{M}$ Taxol) held by three optically trapped anchor points (bead $i = 1$, beads $j = 2, 3$) revealed an unexpected elastic behavior. Relative to the first bead connection $1 \rightarrow 2$ with one MT, the addition of a second MT makes the new bead connection $1 \rightarrow 3$ five times stiffer in longitudinal direction and five times softer in lateral direction. Hence, longitudinal momentum can be well transported through this linear construct, but lateral momentum is damped such that the linear construct acts as angular filter for the transport of mechanical momentum. Remarkably, the single filament description of the elastic modulus $G'(\omega)$ as the sum of a frequency independent part $G'(0)$ and a part following a power law is still valid and the transition frequency for longitudinal momentum transport also increases with increasing $G'(0)$. Since longitudinal and lateral tubulin bonds differ in strength, one can conclude that the geometry of the network and the angular direction of momentum transport affect the molecular relaxation behavior of individual tubulin heterodimers and the stabilizing molecules bound to these heterodimers.

The two-step elastic modulus $G^{(1,3)}$ can be modelled as serial connection of two springs, resulting in an additional coupling term G_{cpl} as explained in the Methods section. It is likely that $G_{cpl}'(\omega, q, F_{ext})$ depends on an external force F_{ext} , which is given in our case by the optically trapped bead 2. The stronger this external (optical) force, the less lateral oscillations can be transferred from the first to the second microtubule, and the stiffer is the connection in longitudinal direction. This trapping effect has been quantified for different stiffnesses of the optical trap as shown in the Fig. 4d, but has not yet been subtracted to obtain the pure elasticity of the filament itself. In general, we have no control of the attachment of both filaments to the second, intermediate bead 2. They might attach perfectly opposite to each other or nearly at the same location giving rise to different effective suspensions of the middle bead.

The role of the intermediate (trapped) bead simulates the situation inside a cell, where filaments are cross-linked to each other, and to other cellular components, such as actin. These crosslinkers have different elasticities, hence, we can test the situation *in vivo* by varying the trap stiffness of the intermediate bead. A recent theoretical study investigated the role of crosslinkers in reversibly crosslinked networks of semi-flexible polymer filaments and found a qualitatively similar behavior, i.e., a low frequency plateau depending on the number of crosslinkers and a power law rise at high frequencies⁴⁹.

Interestingly, this situation resembles an (electronic) transistor, where a small input signal (here, a mechanical stimulus) controls a strong current (here, the momentum transport from bead 1 \rightarrow 3). It will be interesting to perform further experimental and theoretical investigations to explain the elastic behavior, where momentum transport between two network nodes can be steered by an intermediate node.

The MT triangle – a uni-directional stable network. Displacement of the actor bead in either radial x- or tangential y- direction as illustrated in Fig. 5 results in a very direct and efficient transport of momentum in direction towards the one or the other sensor bead. Remarkably, the measured elasticity behavior described by the modulus $G'(\omega)$ is the same as in the single filament case. It consists of a static elasticity $G'(0)$, and a strong rise of $G'(\omega)$ when higher deformation modes are excited beyond the transition frequency ω_t . This strong rise is clearly visible at $f_t = 100$ Hz for a tangential oscillation, but could not be resolved for a radial oscillation. This is probably due to a much faster rise (larger exponent) of G' in a direction lateral to the filament axis, as we observed this phenomenon for single filaments and the linear MT chain as well. However, based on our observations for single filaments, we could estimate the transition frequency for a radial oscillation of the triangle to be $f_t \approx 800$ Hz.

In the static case, the triangle is about 25 times stiffer than a single filament. This can be explained by the fact that every radial or tangential displacement of the actor bead results in a compression and stretching of another MT at the same time. Since MTs are hardly stretchable³², this results in static elasticities of $G'(0) \approx 20\text{--}50$ mPa. Comparing the estimates for the transition frequency ω_t obtained from $G'(0)$ and Equation (3), these extrapolated values come close to the frequency where $G'(\omega) \approx 1.5 \cdot G'(0)$. Again, we interpret the increased transition frequency as a result of the intermolecular relaxations of or between two tubulin heterodimers, which cannot follow on timescales below $2\pi/\omega_t < 10$ ms. A stiffening beyond a transition frequency of $f_t \approx 200$ Hz could also be observed in cross-linked actin networks⁵⁰.

Whereas the optically trapped anchor points could rotate and act as hinges in the previous configurations, the anchor points of the triangle can hardly rotate, and therefore rather resemble a movable support only. This triangular situation is relevant for the radial MT arrays that form around the nuclei of many cells by a mechanism where microtubule-nucleation factors are directionally transported by dynein motors⁵¹. In addition, the forces conveyed to the nucleus by this network would act, via links of the cytoskeleton to the nuclear lamina, on structure and dynamics of the chromatin⁵², providing a mechanism how mechanic signals can modulate gene activity in the network's center.

Summary and conclusions. Motivated by the capability of individual microtubules and inter-connected microtubule networks to transduce a mechanical stimulus over a long distance within short times, we clearly identified substantial differences in response for different network topologies and at different stimulation frequencies ω ³⁵. This has a couple of interesting implications for biology:

The rather low stiffness at frequencies below the characteristic transition frequency, $\omega < \omega_t$, of single filaments or the linear network is expected to dampen the transmission of mechanical signals, while the rise at $\omega > \omega_t$ would allow for an enhanced transmission of signals that typically show a reduced amplitude in noise driven systems such as living cells.

Interestingly, this transition frequency is in a physiologically relevant range (1–10 Hz). For instance, the mammalian heartbeat ranges between 1 Hz in humans up to 18 Hz in mice⁵³, and muscles undergo an innate oscillation of around 20 Hz⁵⁴.

A second aspect of the strong influence of network topology is the comparatively high stiffness at low frequencies of triangular networks. This displays a stiff, load bearing scaffold, which could be used to reinforce the cell against external pressure in densely packed tissues, or enable the contraction of large scale MT networks⁵⁵. The specific mechanical properties of triangular networks are relevant for nuclear positioning, since the nucleus is tethered and positioned by radial arrays that are stabilized by cross-connection in many organisms integrated into cell polarity⁵⁶. A third implication of our findings is linked with the “mechanic transistor” function of microtubule networks, where small mechanical forces can control a large amount of momentum transport.

Microtubule crosslinkers have recently been reported to be able to generate entropic forces on the pN range⁵⁷, which could lead to passive changes of network elasticity over time by pre-stretching individual filaments of a network. This would provide a mechanism how cells can control the directionality of mechanic signaling, which is relevant for mechanic integration of cells into organs, or of organs into organisms². These implications show that our bottom-up approach to analyze the transmission of mechanic forces in networks of increasing complexity is relevant to understand, how mechanic signals can shape biology.

Materials and Methods

Theoretical description of viscoelastic behavior. This section introduces the relevant forces acting on a single filament and its resulting deformations as well as the relative bead displacements during an oscillation longitudinal to the MT. Through a representation of all forces in frequency space, the elastic and viscous components of the filament can be extracted using the frequency dependent complex shear modulus $G(\omega)$.

To separate the viscoelastic contributions of the filament and the trapped beads, we analyzed the data by means of active two particle micro-rheology in frequency space. Because the microtubule is firmly attached to the beads, every displacement x_b of a bead in x direction directly results in an evasion of the microtubule, i.e., buckling with amplitude $u(x, x_b)$. Hence, the forces acting on the microtubule and the forces on the beads are directly coupled through the constraint of a constant contour length L . As we show in the Supplementary Results, the measured net forces on the beads in direction lateral (y) to the filament are negligibly small, such that all effective forces due to microtubule buckling and viscous drags point only in x direction. Hence, in the tension free case the sum of forces acting on a single bead with index j can be described by the following, one dimensional equation of motion for the bead at longitudinal position x_{B_j} and the filament contour described by $u(x)$:

$$F_{optj}(x_{Bj}) + F_{\gamma_B}(x_{Bj}) + \frac{1}{2}F_{\kappa_{MT}}(u(x)) + \frac{1}{2}F_{\gamma_{MT}}(u(x)) = F_D \quad (4)$$

Here, $F_{optj} \approx -\kappa_T(x_{Bj}(t) - x_{Lj}(t))$ is the elastic optical force and $F_{\gamma_{Bj}} \approx -\gamma_B \frac{\partial}{\partial t} x_{Bj}(t)$ with $\gamma_B = 6\pi R_B \eta$ the translational viscous drag force both acting on bead j and balancing the counteracting elastic buckling force $F_{\kappa_{MT}} = \int_0^L EI \cdot \left| \frac{\partial^4}{\partial x^4} u(x, t) \right| dx^{33}$ and the viscous drag force $F_{\gamma_{MT}} \approx \int_0^L g_{MT} \cdot \frac{\partial}{\partial t} |u(x, t)| dx$ of the MT filament integrated along the contour length L and with bending modulus (flexural rigidity) $EI = k_B T \cdot l_p$, where l_p is the persistence length of the semiflexible polymer with $L \ll l_p$. $g_{MT} = \frac{4\pi\eta}{\ln(L/D) + 0.84}$ is the lateral viscous drag coefficient per unit length, and η the viscosity of water⁵⁸. Both in our theoretical description as well as in our rheological analysis shown in Figs 3, 4 and 6, we only include the effects of buckling during single filament compression, and neglect microtubule stretching because the microtubule stretching spring constant is on the order of 10 pN/nm³². This would result in a maximal extension during our experiments of approximately 1 nm, compared to large buckling deformations on the order of several 100 nm. The absolute values in the expressions for the total buckling and viscous forces of the filament are due to symmetry: filament buckling in positive or negative direction $\pm u(x)$ must always result in the same force on the beads.

The oscillatory driving force $F_D(t) = -\kappa_T \cdot x_{L1}(t)$ is generated by the first optical trap ($j = 1$, actor trap) at position $x_{L1}(t) = A_1 \sin(\omega_d t)$, thereby compressing and stretching the MT. The equation of motion according to Equation (4) can then be given explicitly:

$$-\left(\kappa_T + \gamma_B \frac{\partial}{\partial t}\right) x_{Bj}(t) \pm \frac{1}{2} \int_0^L \left[EI \left| \frac{\partial^4}{\partial x^4} u(x, t) \right| + g_{MT} \frac{\partial}{\partial t} |u(x, t)| \right] dx = -\kappa_T A_1 \sin(\omega_d t) \quad (5)$$

Hence, Equation (5) represents a set of m coupled differential equations, where m is the number of beads. These are solved pair wise using relative and collective coordinates $x_R = x_{B1} - x_{B2}$ and $x_C = x_{B1} + x_{B2}$. Since the contribution of the filament acts in opposite directions for each bead (points away from the MT ends, \pm in Equation (5)), this effect cancels out in the collective coordinate $x_C(x_{B1}, x_{B2})$, but manifests in the relative coordinate $x_R(x_{B1}, x_{B2}, u)$.

The buckling of the filament contour $u(x_{B1}, x_{B2}, x, t)$ is a function of the compression given by the bead positions x_{B1} and x_{B2} and is assumed to be deformed in lateral direction y only with small angles to the x -axis. The deformation amplitude can be written as a superposition of sinusoidal modes with wavenumber $q_n = n \cdot \pi / L$ ($n \geq 1$)^{59–61}:

$$u(x, t) = \sum_{n=1}^N u_{qn}(t) \cdot \sin(q_n x) \quad (6)$$

The amplitudes $u_{qn}(t) = \frac{1}{n\pi} \sqrt{2L\delta_L(t) - \delta_L^2(t)}$ of these modes decay exponentially with time according to the temporal auto-correlation function $AC[u(x, t)] = \frac{L}{2q_n^4 \ell_p} \exp(-\omega_{qn} t)$ and can be estimated considering the constant arc length $L = \int_0^{L-\delta_L} \sqrt{1 + \left(\frac{\partial}{\partial x} u(x, t)\right)^2} dx$ of the buckled MT. The filament is axially compressed by $\delta_L(t) \approx x_{L1}(t)$, which is a reasonable approximation to the resulting elliptic integral, as shown in the Supplementary Results. The mode relaxation with frequency $\omega_{qn} = \frac{EI}{g_{MT}} q_n^4$ is the faster, the larger the wave number and the bending modulus EI . For a single deformation mode q_n , Equation (5) then becomes for the relative coordinate x_R

$$-\left(\kappa_T + \gamma_B \frac{\partial}{\partial t}\right) \cdot x_R(t) + \left(EI \cdot q_n^4 + g_{MT} \frac{\partial}{\partial t}\right) \cdot u_{qn}(t) \int_0^L |\sin(q_n x)| dx = F_D(t) \quad (7)$$

with $\int_0^L |\sin(q_n x)| dx = n \int_0^{L/n} \sin\left(\frac{n\pi}{L} x\right) dx = \frac{2 \cdot n}{q_n}$. Using the temporal frequency ω and the Fourier relation $\frac{\partial}{\partial t} \rightarrow i\omega$, Equation (7) reads in frequency space:

$$-\left(\kappa_T + i\omega\gamma_B\right) \cdot \tilde{x}_R(\omega) + \left(2EI \cdot nq_n^3 + 2i\omega g_{MT} \frac{n}{q_n}\right) \cdot \tilde{u}_{qn}(\omega) = \tilde{F}_D(\omega) \quad (8)$$

The spectral forces acting on the beads with relative position $\tilde{x}_R(\omega)$ are known and can be subtracted, such that the following response equation holds: $\tilde{u}_{qn}(\omega) = \alpha_{qn}(\omega) \Delta \tilde{F}_D(\omega)$. Here, $\Delta \tilde{F}_D(\omega)$ is the Fourier transform of the external force $F_D(t) + \left(\kappa_T + \gamma_B \frac{\partial}{\partial t}\right) x_R(t)$, which deforms the MT at different temporal and spatial frequencies.

$\alpha_{qn}(\omega) = \left(2EI \cdot nq_n^3 + 2i\omega g_{MT} \frac{n}{q_n}\right)^{-1}$ is the end-to-end response function of a single microtubule deflected by $\tilde{u}_{qn}(\omega)$ upon $\tilde{F}_D(\omega)$, which simplifies to $\alpha_{qn}(\omega) = (2EI)^{-1} \cdot \left(nq_n^3 + inq_n^3 \frac{\omega}{\omega_n}\right)^{-1} = \left(2kT \cdot \ell_p nq_n^3\right)^{-1} \cdot \left(1 + i\frac{\omega}{\omega_n}\right)^{-1}$, with units $[\alpha_{qn}] = \frac{m}{N}$. The total response function over all N deformation modes can be calculated as a superposition of N individual response functions $\alpha(\omega) = \sum_n \alpha_{qn}(\omega)$. Using the wave number $q_1 = \frac{\pi}{L} = \frac{1}{n} q_n$ and the relaxation frequency $\omega_1 = \frac{EI}{g_{MT}} q_1^4 = \frac{1}{n^4} \omega_n$ of the ground mode with $n = 1$, one obtains:

$$\alpha(\omega) = \frac{1}{2q_1^3 kT \ell_p} \sum_{n=1}^N \frac{1}{n^4 + i\omega / \omega_1} \quad (9)$$

with $\alpha(0) = \frac{1}{2q_1^3 k_B T \ell_p} \sum_{n=1}^{\infty} \frac{1}{n^4} = \frac{\pi^4}{180 q_1^3 k_B T \ell_p} = \frac{0.54}{q_1^3 k_B T \ell_p}$. The complex viscoelastic response functions of the MT filament consists of the storage modulus $G'(\omega)$, describing the elastic energy stored in the system, and the loss modulus $G''(\omega)$, describing the friction energy dissipated to the environment. By using $G(\omega) = \frac{1}{4\pi L \cdot \alpha(\omega)}$, we find:

$$G'(\omega > \omega_1) = \text{Re}\left\{\frac{1}{4\pi L \cdot \alpha(\omega > \omega_1)}\right\} \approx C \cdot \omega^p \quad (10)$$

$$\frac{1}{1.86} G'(\omega_1) = G'(\omega = 0) = \frac{1}{2.16\pi^2} q_1^4 k_B T \ell_p = \frac{1}{2.16\pi^2} g_{MT} \omega_1 \quad (11)$$

And $G''(\omega) = \frac{\text{Im}(\alpha(\omega))}{|\alpha(\omega)|} \approx \frac{\eta\omega}{\ln(L/D) + 0.84}$ where C is a constant factor. For higher driving frequencies $\omega > \omega_1$, $G'(\omega)$ follows a power law with $p = 3/4$ ⁵⁹, whereas a more advanced theory for semiflexible filaments^{36, 37} predicts a power law with $p = 5/4$. For low frequencies $\omega \rightarrow 0$, the elastic modulus is close to the first mode $G'(\omega_{n=1})$, which is independent of the frequency.

In the following, we only investigate the elastic component G' , whereas the viscous contributions G'' , expressed by the viscous drag g_{MT} of the MT, are discussed in the Supplementary Results.

Theoretical estimate for MT stiffening on short timescales. The question is how well our observations can be explained on the basis of an equation of forces, as introduced in Equation (4), and viscoelastic forces known from hydrodynamic beam theory. Our theoretical description of microtubule deformation through the shear modulus $G'(\omega)$ is based on the beam equation $M(x) = EI \frac{d^2\theta(x)}{dx^2}$ with bending moment M and tangent angle $\theta(x)$ along the filament⁵⁸, which has been successfully applied to active filament stretching³² and buckling³¹ and to thermal deformations³³. On this basis, the static MT deformations result in a strong length dependency of $G'(\omega = 0) \sim \left(\frac{1}{L}\right)^4$. However, by considering the contour-length dependence of the persistence length $l_p(\omega = 0, L) \sim L^2$ ³⁸, the plateau value $G'(0)$ as well as the transition frequency ω_t approximate to a $\left(\frac{1}{L}\right)^2$ dependency. Whereas this could be confirmed for the plateau value, the description of the transition frequency requires a more advanced theory, which should also include the molecular architecture of differently stabilized filaments.

As introduced above, the buckling amplitude of the filament deformation $u(x_{B1}, x_{B2}, t)$ is a superposition of different deformation modes, which relax the faster, the larger the wave number $q_n = n \cdot \pi/L$, or the shorter the deformation length. By calculating individual response functions $\alpha(\omega, q)$ for each mode q_n and taking the inverse sum of all response functions, $G'(\omega, n) = 1/(\sum_n \alpha(\omega, q))$, both the elastic and viscous modulus are obtained. It turned out that typically $n = 4$ modes were excited at our maximum driving frequency of 100 Hz, such that the fit function $G'_{fit}(\omega) = \frac{3(59\omega^6 + 1383427\omega_1^2\omega^4 + 1520884952\omega_1^4\omega^2 + 19790659584\omega_1^6)}{2A(4\omega^6 + 176037\omega_1^2\omega^4 + 511196337\omega_1^4\omega^2 + 32023818304\omega_1^6)} \approx G'(\omega, n = 4)$ with the parameters A and ω_1 was sufficient.

Using this fit function, the transition frequency $\omega_t \approx 3\omega_1$ could be extracted from the experimental data. ω_t was interpreted as the frequency at which molecular relaxations cannot follow the external filament deformation. The frequency independent stiffness at low frequencies and the sudden increase in $G'(\omega)$ on a double-logarithmic scale could be well observed in single filaments as well as in the linear and triangular MT arrangements. From these observations, we conclude that the description of forces chosen in Equations (4) and (5) to quantify our mechanistic model is reasonable. However, the stronger stiffening at high frequencies with $p > 5/4$ needs a more thorough theoretical investigation. In addition, the theoretical approach has to be extended in the future, to also integrate the porous molecular structure, especially to explain the dependence of the transition frequency on chemical stabilization of the microtubule (see Supplementary Results).

Stiffness estimate for a linear MT chain. The two-step elastic modulus $G'^{(1,3)}$, resulting in a fivefold stiffening in longitudinal direction and fivefold softening in lateral direction compared to the one-step modulus $G'^{(1,2)}$, can be modelled as serial connection of two springs (two filaments, $2l$) with MT length $L/2$ or wave number $2q$, such that $G'^{(1,3)} \rightarrow G'_{2fl}(2q)$. Reciprocal addition of two single filament elasticities $G'_{1f}(2q)$ results in a two filament sum elasticity, $G'_{2fl}(0, 2q) = \left(\frac{1}{G'_{1f}(0, 2q)} + \frac{1}{G'_{1f}(0, 2q)}\right)^{-1} = \frac{1}{2} G'_{1f}(0, 2q) \neq G'^{(1,3)}(0, 2q)$, which is two times softer than that of a single filament. Alternatively, the two-step modulus $G'^{(1,3)}$ can be identified with a single filament of length L , or wave number q , such that $G'^{(1,3)} \rightarrow G'_{1f}(q)$. However, this results in a fivefold decrease of the elasticity relative to that of a single filament with length $L/2$, according to $G'_{1f}(0, 2q) = l_p(0, 2q) k_B T (2q)^4 = \frac{16}{3} l_p(0, q) k_B T q^4 \approx 5 \cdot G'_{1f}(0, q)$. The factor $1/3$ arises from the length dependence of $l_p(q)$.

Hence, an additional coupling term G'_{cpl} is required to explain the elastic behavior of the linear construct, such that

$$G'^{(1,3)}(\omega, q) = G'_{1f}(\omega, q) + G'_{cpl}(\omega, q) \quad (12)$$

$G'_{cpl}(0, q)$ must be positive for longitudinal momentum transport, and negative for lateral momentum transport.

Experimental setup with optically trapped beads as actor and sensor. A single biotinylated microtubule was attached laterally to two Neutravidin coated beads trapped by time-multiplexed optical tweezers and aligned along the x-direction as illustrated in Fig. 1. The average laser power per trap was always 19 mW in the focal plane at a trapping wavelength of 1064 nm. The position of each bead was tracked in three dimensions at

50 kHz using back focal plane (BFP) interferometry and quadrant photo diodes (QPD) as described in ref. 62. The first optical trap (trap 1, shown in red) was the force generating actor and oscillates sinusoidally at frequency f_a and amplitude A_a along x around the central position x_{01} . The other trap(s) (blue) remained static and were used as position and force sensors for the mechanical stimulus exerted by the actor and transduced by the microtubule. The beads were displaced by x_{B1} and x_{B2} relative to the trap centers. During both half periods of an oscillation, the distance between the beads was first increased and then decreased resulting in tensile and compressive forces acting on the microtubule, respectively. Since microtubules are practically inextensible, they are bent locally at the point of attachment to beads (Fig. 1a) during the first half period³² and buckled during the second half period due to their high compliance to compression forces⁶³. The buckling amplitude along the filament is denoted by $u(x, t)$ as illustrated in Fig. 1c.

In the experiments, we used a lateral stiffness of $\kappa_{opt} \approx 25 \text{ pN}/\mu\text{m}$ per trap. The actor trap was typically oscillating at frequencies $0.1 \text{ Hz} \leq f_a \leq 100 \text{ Hz}$ in nearly logarithmical steps and amplitudes $200 \text{ nm} \leq A_a \leq 600 \text{ nm}$ along x or y , i.e., longitudinal or lateral with respect to the axis of single filaments or the linear chain. Each filament or construct was probed several times at different amplitudes to test for any force or displacement dependence, to obtain statistics, and to test for structural defects during experiments, which happened rarely and usually resulted in filament breaking close to one bead. In such cases, the measurements were excluded from further analysis. Also, we did not observe significant differences for repetitive measurements on the same filament indicating that microtubules were not structurally damaged during oscillation. In some cases, one of the filaments was detached of a bead. These experiments have also been excluded from analysis. Elastic effects of the biotin linker can be neglected, since the effective length of this linker is in the Ångström range⁶⁴ and its spring constant^{65, 66} is much larger than that of microtubules, both for buckling and stretching³².

Suitability of experimental approach. The use of optically trapped beads as anchor points for simple microtubule networks turned out to be a very suitable approach. Potential phototoxic effects such as bleaching and filament breaking were successfully suppressed by addition of glucose oxidase and catalase as enzymatic scavengers of reactive oxygen species (see Microtubule preparation), which allowed to obtain reproducible results for more than 30 experimental repeats on the same construct extending up to 40 minutes. At a moderate laser power of 19 mW per trap, optical forces were high enough to compensate all occurring friction and elastic forces. Only for trap displacements at frequencies strongly exceeding 100 Hz, the trapping of higher refracting polystyrene spheres became unstable⁶⁷. However, most physiologically relevant mechanical forces on timescales below $(100 \text{ Hz})^{-1} = 10 \text{ ms}$ are local effects on the order of one pN or less, caused by thermal fluctuations and are likely not relevant for a transport through the entire cell. As we have shown in the Supplementary Results, the extents of the $1 \mu\text{m}$ large beads result in additional geometrical effects affecting the deformation and have to be considered in the future. However, these effects are minor and do not impair the feasibility of the strategy to use individually trapped beads as flexibly controllable force actors and sensors within small MT networks. The basis for all experiments were the multi-particle trapping, the precise position tracking and the force measurement in well calibrated optical traps, which worked robustly at the used tracking rates of $50 \text{ kHz}/N$ (N = number of traps). We think that this successful approach for optical trapping and tracking of anchor points will also allow investigating more complicated networks in the future.

Microtubule preparation. Tubulin was purified from fresh brains collected freshly after slaughtering using the classical protocol by Shelanski *et al.*⁶⁸. For biotinylation, microtubules were preassembled at 37°C in presence of $100 \mu\text{M}$ taxol and $100 \mu\text{M}$ of GTP in BRB80 buffer (80 mM Pipes KOH, pH 6.8, 1 mM MgCl_2 , 1 mM EGTA), and then complemented with $500 \mu\text{M}$ of sodium bicarbonate and 1 mg/ml of biotin-XX N-hydroxysuccinimide ester. After incubation for 30 min at 37°C , the mixture was purified by ultracentrifugation through a twofold volume of a sucrose cushion (15 min 300000 g) in BRB80. Purity and quality of each tubulin preparation was verified by SDS-PAGE, before coupling the purified tubulin to tetramethyl rhodamine as described previously⁶⁹. For Taxol stabilized microtubules, tubulin, fluorescently labeled tubulin, and biotinylated tubulin were thawed on ice, mixed with GTP in the ratio 8: 4: 4: 0.8 and polymerized for 30 min at 37°C . This stock was stable up to 2 days at room temperature. Dilutions (1:100 – 1:2000) in BRB80 buffer containing Taxol ($10 \mu\text{M}$ or $100 \mu\text{M}$) were prepared freshly from the stock every 2–3 hours during experiments. Doubly stabilized filaments were polymerized similarly, but with Guanosine-5'-[(α , β)-methylene]triphosphate (GMPCPP) instead of GTP and spun down with a TLA100 rotor in a Beckman centrifuge at 300000 g . Sedimented microtubules were resuspended in BRB80 buffer containing $100 \mu\text{M}$ Taxol and stable for 2–3 months at room temperature. Further dilutions (1:100 – 1:500) were prepared freshly during experiments. $7.5 \mu\text{l}$ of the microtubule suspension was mixed on a coverslip with Neutravidin coated beads (Molecular probes, Invitrogen, F8777), and an oxygen scavenging system (GODCAT, $100 \mu\text{g/ml}$ Glucose oxidase 22778 from Serva, $20 \mu\text{g/ml}$ catalase C40 from Sigma, 10 mM BME M3148 from Sigma and 40 mM Glucose from Carl Roth) to prevent fluorescence bleaching and filament breaking. We always used a roughly $80 \mu\text{m}$ thick coverslip sandwich separated by double sided sticky tape (Tesa).

References

- Orr, A. W., Helmke, B. P., Blackman, B. R. & Schwartz, M. A. Mechanisms of mechanotransduction. *Developmental cell* **10**, 11–20 (2006).
- Hamant, O. *et al.* Developmental patterning by mechanical signals in Arabidopsis. *Science* **322**, 1650–1655 (2008).
- Jaalouk, D. E. & Lammerding, J. Mechanotransduction gone awry. *Nature Reviews Molecular Cell Biology* **10**, 63–73 (2009).
- Chin, L., Xia, Y., Discher, D. E. & Janmey, P. A. Mechanotransduction in cancer. *Current Opinion in Chemical Engineering* **11**, 77–84 (2016).
- Shivashankar, G. Mechanosignaling to the cell nucleus and gene regulation. *Annual review of biophysics* **40**, 361–378 (2011).
- Maniotis, A. J., Chen, C. S. & Ingber, D. E. Demonstration of mechanical connections between integrins, cytoskeletal filaments, and nucleoplasm that stabilize nuclear structure. *Proceedings of the National Academy of Sciences* **94**, 849–854 (1997).

7. Na, S. *et al.* Rapid signal transduction in living cells is a unique feature of mechanotransduction. *Proceedings of the National Academy of Sciences* **105**, 6626–6631 (2008).
8. Ingber, D. E. The riddle of morphogenesis: a question of solution chemistry or molecular cell engineering? *Cell* **75**, 1249–1252 (1993).
9. Wang, N., Tytell, J. D. & Ingber, D. E. Mechanotransduction at a distance: mechanically coupling the extracellular matrix with the nucleus. *Nature Reviews Molecular Cell Biology* **10**, 75–82 (2009).
10. Huber, F. *et al.* Emergent complexity of the cytoskeleton: from single filaments to tissue. *Advances in Physics* **62**, 1–112 (2013).
11. Haase, K. *et al.* Extracellular Forces Cause the Nucleus to Deform in a Highly Controlled Anisotropic Manner. *Scientific reports* **6**, 21300 (2016).
12. Shao, X., Li, Q., Mogilner, A., Bershadsky, A. D. & Shivashankar, G. Mechanical stimulation induces formin-dependent assembly of a perinuclear actin rim. *Proceedings of the National Academy of Sciences* **112**, E2595–E2601 (2015).
13. Liang, X., Madrid, J. & Howard, J. The Microtubule-Based Cytoskeleton Is a Component of a Mechanical Signaling Pathway in Fly Campaniform Receptors. *Biophysical Journal* **107**, 2767–2774 (2014).
14. Brangwynne, C. P. *et al.* Microtubules can bear enhanced compressive loads in living cells because of lateral reinforcement. *The Journal of cell biology* **173**, 733–741 (2006).
15. Nick, P. Microtubules, signalling and abiotic stress. *The Plant Journal* **75**, 309–323 (2013).
16. Savage, C. *et al.* *mec-7* is a beta-tubulin gene required for the production of 15-protofilament microtubules in *Caenorhabditis elegans*. *Genes & development* **3**, 870–881 (1989).
17. Bergman, J., Osunbayo, O., Vershinin, M. Constructing 3D microtubule networks using holographic optical trapping. *Scientific reports* **5**, (2015).
18. Mohrdieck, C. *et al.* Biomimetic models of the actin cytoskeleton. *Small* **3**, 1015–1022 (2007).
19. Uhrig, K. *et al.* Optical force sensor array in a microfluidic device based on holographic optical tweezers. *Lab on a chip* **9**, 661–668 (2009).
20. Vignaud, T., Blanchoin, L. & Théry, M. Directed cytoskeleton self-organization. *Trends in cell biology* **22**, 671–682 (2012).
21. Ahmed, W. W., Fodor, É. & Betz, T. Active cell mechanics: Measurement and theory. *Biochimica et Biophysica Acta (BBA)-Molecular Cell Research* (2015).
22. Atakhorrami, M. *et al.* Correlated fluctuations of microparticles in viscoelastic solutions: quantitative measurement of material properties by microrheology in the presence of optical traps. *Physical Review E* **73**, 061501 (2006).
23. Mizuno, D., Head, D., MacKintosh, F. & Schmidt, C. Active and passive microrheology in equilibrium and nonequilibrium systems. *Macromolecules* **41**, 7194–7202 (2008).
24. Gardel, M. *et al.* Scaling of F-actin network rheology to probe single filament elasticity and dynamics. *Physical Review Letters* **93**, 188102 (2004).
25. Xu, J., Palmer, A. & Wirtz, D. Rheology and microrheology of semiflexible polymer solutions: actin filament networks. *Macromolecules* **31**, 6486–6492 (1998).
26. Pelletier, V., Gal, N., Fournier, P. & Kilfoil, M. L. Microrheology of microtubule solutions and actin-microtubule composite networks. *Physical Review Letters* **102**, 188303 (2009).
27. Brangwynne, C. P., MacKintosh, F. & Weitz, D. A. Force fluctuations and polymerization dynamics of intracellular microtubules. *Proceedings of the National Academy of Sciences* **104**, 16128–16133 (2007).
28. Chen, D. *et al.* Two-Bubble Acoustic Tweezing Cytometry for Biomechanical Probing and Stimulation of Cells. *Biophysical Journal* **108**, 32–42 (2015).
29. Guo, M. *et al.* Probing the stochastic, motor-driven properties of the cytoplasm using force spectrum microscopy. *Cell* **158**, 822–832 (2014).
30. Hoffman, B. D., Massiera, G., Van Citters, K. M. & Crocker, J. C. The consensus mechanics of cultured mammalian cells. *Proceedings of the National Academy of Sciences* **103**, 10259–10264 (2006).
31. Kurachi, M., Hoshi, M. & Tashiro, H. Buckling of a single microtubule by optical trapping forces: direct measurement of microtubule rigidity. *Cell motility and the cytoskeleton* **30**, 221–228 (1995).
32. van Mameren, J., Vermeulen, K. C., Gittes, F. & Schmidt, C. F. Leveraging Single Protein Polymers To Measure Flexural Rigidity†. *The Journal of Physical Chemistry B* **113**, 3837–3844 (2009).
33. Gittes, F., Mickey, B., Nettleton, J. & Howard, J. Flexural rigidity of microtubules and actin filaments measured from thermal fluctuations in shape. *The Journal of cell biology* **120**, 923–934 (1993).
34. Brangwynne, C. P. *et al.* Bending dynamics of fluctuating biopolymers probed by automated high-resolution filament tracking. *Biophysical Journal* **93**, 346–359 (2007).
35. Lopez, B. J. & Valentine, M. T. Molecular control of stress transmission in the microtubule cytoskeleton. *Biochimica et Biophysica Acta (BBA)-Molecular Cell Research* **1853**, 3015–3024 (2015).
36. Pasquali, M., Shankar, V. & Morse, D. C. Viscoelasticity of dilute solutions of semiflexible polymers. *Physical Review E* **64**, 020802 (2001).
37. Shankar, V., Pasquali, M. & Morse, D. C. Theory of linear viscoelasticity of semiflexible rods in dilute solution. *Journal of Rheology (1978-present)* **46**, 1111–1154 (2002).
38. Pampaloni, F. *et al.* Thermal fluctuations of grafted microtubules provide evidence of a length-dependent persistence length. *Proceedings of the National Academy of Sciences of the United States of America* **103**, 10248–10253 (2006).
39. Hawkins, T., Mirigian, M., Selcuk Yasar, M. & Ross, J. L. Mechanics of microtubules. *Journal of biomechanics* **43**, 23–30 (2010).
40. Taute, K. M., Pampaloni, F., Frey, E. & Florin, E.-L. Microtubule dynamics depart from the wormlike chain model. *Physical Review Letters* **100**, 028102 (2008).
41. Poirier, M. G. & Marko, J. F. Effect of internal friction on biofilament dynamics. *Physical Review Letters* **88**, 228103 (2002).
42. Ziebert, F., Mohrbach, H. & Kulić, I. M. Why Microtubules Run in Circles: Mechanical Hysteresis of the Tubulin Lattice. *Physical Review Letters* **114**, 148101 (2015).
43. Ziebert, F., Mohrbach, H. & Kulić, I. M. A nonequilibrium power balance relation for analyzing dissipative filament dynamics. *The European Physical Journal E* **38**, 1–8 (2015).
44. Hawkins, T. L., Sept, D., Mogessie, B., Straube, A. & Ross, J. L. Mechanical properties of doubly stabilized microtubule filaments. *Biophysical journal* **104**, 1517–1528 (2013).
45. Maurer, S. P., Fourniol, F. J., Bohner, G., Moores, C. A. & Surrey, T. EBs recognize a nucleotide-dependent structural cap at growing microtubule ends. *Cell* **149**, 371–382 (2012).
46. Lopez, B. J. & Valentine, M. T. Mechanical effects of EB1 on microtubules depend on GTP hydrolysis state and presence of paclitaxel. *Cytoskeleton* **71**, 530–541 (2014).
47. Pampaloni, F. & Florin, E.-L. Microtubule architecture: inspiration for novel carbon nanotube-based biomimetic materials. *Trends in biotechnology* **26**, 302–310 (2008).
48. Tuszyński, J., Luchko, T., Portet, S. & Dixon, J. Anisotropic elastic properties of microtubules. *The European Physical Journal E: Soft Matter and Biological Physics* **17**, 29–35 (2005).
49. Plagge, J., Fischer, A. & Heussinger, C. Viscoelasticity of reversibly crosslinked networks of semiflexible polymers. *arXiv preprint arXiv:160203343* (2016).

50. Koenderink, G., Atakhorrami, M., MacKintosh, F. & Schmidt, C. High-frequency stress relaxation in semiflexible polymer solutions and networks. *Physical Review Letters* **96**, 138307 (2006).
51. Vorobjev, I., Malikov, V. & Rodionov, V. Self-organization of a radial microtubule array by dynein-dependent nucleation of microtubules. *Proceedings of the National Academy of Sciences* **98**, 10160–10165 (2001).
52. Ramdas, N. M. & Shivashankar, G. Cytoskeletal control of nuclear morphology and chromatin organization. *Journal of Molecular Biology* **427**, 695–706 (2015).
53. Vornanen, M. Maximum heart rate of soricine shrews: correlation with contractile properties and myosin composition. *American Journal of Physiology-Regulatory, Integrative and Comparative Physiology* **262**, R842–R851 (1992).
54. Jewell, B. & Ruegg, J. Oscillatory contraction of insect fibrillar muscle after glycerol extraction. *Proceedings of the Royal Society of London B: Biological Sciences* **164**, 428–459 (1966).
55. Foster, P. J., Fürthauer, S., Shelley, M. J. & Needleman, D. J. Active contraction of microtubule networks. *eLife*, e10837 (2015).
56. Morris, N. R. Nuclear positioning: the means is at the ends. *Current opinion in cell biology* **15**, 54–59 (2003).
57. Lansky, Z. *et al.* Diffusible crosslinkers generate directed forces in microtubule networks. *Cell* **160**, 1159–1168 (2015).
58. Howard, J. *Mechanics of Motor Proteins and the Cytoskeleton* (2001).
59. Gittes, F. & MacKintosh, F. Dynamic shear modulus of a semiflexible polymer network. *Physical Review E* **58**, R1241 (1998).
60. Li, T. A mechanics model of microtubule buckling in living cells. *Journal of biomechanics* **41**, 1722–1729 (2008).
61. Feynman, R. P., Leighton, R. B. & Sands, M. The Feynman lectures on physics, vol. 2: Mainly electromagnetism and matter. Addison-Wesley (1979).
62. Ruh, D., Traenkle, B. & Rohrbach, A. Fast parallel interferometric 3D tracking of numerous optically trapped particles and their hydrodynamic interaction. *Optics Express* **19**, 21627–21642 (2011).
63. Kikumoto, M., Kurachi, M., Tosa, V. & Tashiro, H. Flexural rigidity of individual microtubules measured by a buckling force with optical traps. *Biophysical journal* **90**, 1687–1696 (2006).
64. Wong, J., Chilkoti, A. & Moy, V. T. Direct force measurements of the streptavidin–biotin interaction. *Biomolecular engineering* **16**, 45–55 (1999).
65. de Odrowąż Piramowicz, M., Czuba, P., Targosz, M., Burda, K. & Szymoński, M. Dynamic force measurements of avidin–biotin and streptavidin–biotin interactions using AFM. *Acta Biochimica Polonica* **53**, 93–100 (2006).
66. Lo, Y.-S., Simons, J. & Beebe, T. P. Temperature dependence of the biotin–avidin bond-rupture force studied by atomic force microscopy. *The Journal of Physical Chemistry B* **106**, 9847–9852 (2002).
67. Speidel, M., Friedrich, L. & Rohrbach, A. Interferometric 3D tracking of several particles in a scanning laser focus. *Optics Express* **17**, 1003–1015 (2009).
68. Shelanski, M. L., Gaskin, F. & Cantor, C. R. Microtubule assembly in the absence of added nucleotides. *Proceedings of the National Academy of Sciences* **70**, 765–768 (1973).
69. Himmelspach, R., Wymer, C. L., Lloyd, C. W. & Nick, P. Gravity-induced reorientation of cortical microtubules observed *in vivo*. *The Plant Journal* **18**, 449–453 (1999).

Acknowledgements

The authors gratefully acknowledge helpful discussions with Igor Kulic, Falko Ziebert, and Felix Jünger as well as Stefan Diez and Friedrich Schwarz for providing GMPCPP filaments. The project was funded by the Deutsche Forschungsgemeinschaft (DFG), grant RO 3615/2-1 and RO 3615/2-3. The article processing charge was funded by the German Research Foundation (DFG) and the University of Freiburg in the funding programme Open Access Publishing.

Author Contributions

M.K. designed and built the optical setup, performed experiments, analyzed data and prepared figures. N.S. and P.N. contributed microtubules and reagents. P.N. commented on the manuscript and contributed to the Discussion and interpretations of the results. A.R. developed the theory with M.K. M.K. and A.R. wrote the paper. A.R. initiated and supervised the project and obtained financial funding.

Additional Information

Supplementary information accompanies this paper at doi:10.1038/s41598-017-04415-z

Competing Interests: The authors declare that they have no competing interests.

Publisher's note: Springer Nature remains neutral with regard to jurisdictional claims in published maps and institutional affiliations.



Open Access This article is licensed under a Creative Commons Attribution 4.0 International License, which permits use, sharing, adaptation, distribution and reproduction in any medium or format, as long as you give appropriate credit to the original author(s) and the source, provide a link to the Creative Commons license, and indicate if changes were made. The images or other third party material in this article are included in the article's Creative Commons license, unless indicated otherwise in a credit line to the material. If material is not included in the article's Creative Commons license and your intended use is not permitted by statutory regulation or exceeds the permitted use, you will need to obtain permission directly from the copyright holder. To view a copy of this license, visit <http://creativecommons.org/licenses/by/4.0/>.

© The Author(s) 2017